Journal of Geodesy (2019) 93:1559–1569
https://doi.org/10.1007/s00190-019-01269-3

ORIGINAL ARTICLE

Co-seismic displacement and waveforms of the 2018 Alaska earthquake from high-rate GPS PPP velocity estimation

Shuanggen Jin[1,3] · **Ke Su**[1,2]

Received: 7 October 2018 / Accepted: 15 June 2019 / Published online: 24 June 2019

Abstract
For earthquake and tsunami early warning and emergency response, the parameters of earthquakes should be determined rapidly and correctly. The precise displacement time series can be obtained from high-rate GPS precise point positioning (PPP) during the earthquake, but require long convergence time. In this paper, the PPP velocity estimation (PPPVE) approach is applied to estimate the velocity waveforms and integrate to displacement waveforms in real-time scenarios. A case study of the 2018 Alaska earthquake is conducted from 1 Hz GPS data. The accuracy of velocity and displacement waveforms for 1 Hz GPS data is analyzed by comparing PPPVE-derived displacements with kinematic PPP solution. The results indicate that PPP and PPPVE are both capable of detecting seismic displacement waveforms with amplitude of 1 cm horizontally, while PPPVE can detect the displacement waveforms with much faster convergence speed. The mean convergence time of PPPVE for north, east and up components are 19, 22 and 31 s, respectively. The derived ground motion parameters estimate a magnitude of $M_w = 7.97 \pm 0.18$, showing a great consistency and agreement with the seismometer magnitude. The preliminary relationship between the seismic intensity and ground motion parameters is established and evaluated for an auxiliary reference. Furthermore, the permanent displacement induced by the earthquake is obtained from real-time PPPVE approach. The benefits of PPPVE approach for GNSS seismology are demonstrated.

Keywords Co-seismic displacement · High-rate GPS · PPP · Earthquake

1 Introduction

An $M_w = 7.9$ earthquake occurred on January 23, 2018 at 09:31:42 Coordinated Universal Time (UTC) 280 km southeast of Kodiak, Alaska. The earthquake occurred as the result of strike slip faulting within the shallow lithosphere of the Pacific plate. Large earthquakes often occur in southern Alaska, the Pacific-North America plate boundary region. Most of them have occurred on the subduction zone interface between the two plates. The process of the earthquake is poorly understood due to the complicated geological structures in the region. Traditionally, earthquake magnitude is derived from the record of accelerometers or broadband seismometers. Seismometers can be saturated or clipped in the earthquake, meaning that they cannot record the full amplitude of velocity any more. Though the accelerometers do not clip, the displacements derived from the double integration of data may be distorted by the instrumental tilts and rotations (Bilich et al. 2008).

Global Navigation Satellite System (GNSS) plays an important role in long-term crustal deformation monitoring (e.g., Jin and Park 2006; Jin and Wang 2008). High-rate GNSS is an effective tool to retrieve displacements for earthquakes, landslides, volcanic and other deformation activities with the accuracy of a few centimeters (Blewitt et al. 2009). The centimeter level accuracy obtained by real-time kinematic (RTK) positioning was firstly demonstrated by Remondi (1985), and Hirahara (1994) demonstrates as GPS seismology with kinematic GPS. A growing number of high-rate GNSS stations have been installed in recent years around the world. High-rate GNSS can directly estimate the broadband displacements, including static offsets and dynamic

✉ Shuanggen Jin
sgjin@shao.ac.cn; sg.jin@yahoo.com

[1] Shanghai Astronomical Observatory, Chinese Academy of Sciences, Shanghai 200030, China

[2] University of Chinese Academy of Sciences, Beijing 100049, China

[3] School of Remote Sensing and Geomatics Engineering, Nanjing University of Information Science and Technology, Nanjing 210044, China

motions of arbitrarily large earthquake magnitudes (Larson et al. 2003; Bock et al. 2004). GNSS-derived displacements can be used to estimate earthquake magnitude, model finite fault slip and warn the early earthquake or tsunami (Blewitt et al. 2006; Wright et al. 2012). GNSS-derived displacements can provide important and additional information for the study of earthquakes. Two common processing strategies are mainly used in GNSS seismology: RTK (Keller et al. 2001) and precise point positioning (PPP) (Zumberge et al. 1997). For RTK, one or more nearby reference stations are used to remove most biases and recover the integer feature of double-differenced ambiguity parameters. The method results in the effective cancelation of GNSS receiver clock and satellite clock errors, which are common to multiple satellites and stations, respectively. Consequently, high positioning accuracy of a few centimeters can be achieved. For instance, the RTK technique was used to analyze the displacements of the 2011 Tohoku-Oki earthquake by Ohta et al. (2012).

However, the RTK technique requires assigning baselines or overlapping networks and needs many stations for simultaneous observations, which is a significant limitation for the analysis of GNSS data from a great deal of ground stations. Furthermore, RTK can only provide a relative position and the local reference station in relative positioning is also likely to be displaced by the strong seismic event, which might mislead the analysis results. Hence, the reference station should be far away from the focal region in RTK. On the other hand, as the length of GNSS baseline increases, the accuracy of positioning could be reduced because of the impact of satellite ephemeris error and atmospheric effects that cannot be neglected in double-difference mode. Similarly, intermittent station dropouts also complicate RTK.

Alternatively, with the availability of high-rate GNSS observations and precise satellite orbit and clock products, PPP can provide absolute displacements in a global reference frame with a single receiver. PPP technology is flexible and does not need to select the reference stations. Although PPP requires a global network to provide clock and orbit products, the stations utilized in the solution are not affected by the earthquake or small enough that do not bias the clock and orbit product. Plenty of works have applied PPP to measure displacement waveforms (e.g., Kouba 2003, 2005; Shi et al. 2010; Xu et al. 2013). Whereas the major problem of PPP is the long convergence time, it will take up 30–60 min before the positioning errors converge (Li et al. 2015). It still costs 15–20 min to converge when applying the ambiguity resolution technology (Ge et al. 2008).

Colosimo et al. (2011) proposed a variometric approach to estimate co-seismic displacements in real time. The approach, based upon time single differences of the carrier phase observations recorded by a single receiver even single frequency only, estimates the time series of the receiver velocities using the broadcast orbits and clocks. Then, velocities are integrated to provide co-seismic displacements. Since only observations and broadcast orbits and clocks are needed, the velocities and displacements can be estimated on-board the receiver, overcoming the need to transfer all the observations to the data center for real-time processing. The approach causes a new problem that velocities and displacements are drifting due to the effects of errors in orbits and clocks. An assumption of linear drift limits the integration interval. The drift value could be large and cannot fully be removed unless the period of seismic shaking is short. Recently, an improvement of this approach has been proposed to overcome this problem, considering that the effect of the orbit and clock errors are greatly spatially correlated (Fratarcangeli et al. 2018). This improvement seems to give good results at least with moderate magnitude earthquakes, where the displacements are limited and their errors have a higher impact in percentage. Li et al. (2013) proposed a new approach for estimating co-seismic displacements using a single receiver in real time, which was validated using the data collected during the Tohoku-Oki earthquake in Japan. Tu (2013) proposed the approach to rapidly determine the displacements with GPS observations without drifting.

In this paper, the method of PPP velocity estimation (PPPVE) is introduced and used to rapidly determine the co-seismic displacements by integrating the estimated velocity in real-time scenarios in Sect. 2. The kinematic PPP is also introduced for a comparison. The accuracy of derived velocity and displacement waveforms for 1 Hz GPS data collected during the Alaska earthquake is analyzed in Sect. 3. Finally, we determine the earthquake magnitude, establish preliminary relationship between the seismic intensity and the ground motion parameters and obtain permanent deformations from the derived parameters.

2 Methodology

Real-time high-precision satellite orbits and clocks are the key issue for real-time GNSS application. Nowadays, the International GNSS Service (IGS) provides final, rapid and ultra-rapid (IGU) products. The IGU products are available for real-time application since they contain predicted parts. The accuracy of the IGU orbit is 5 cm, but the root-mean-square (RMS) of the IGU satellite clock offset is, unfortunately, about 3 ns (Zhang et al. 2011). The accuracy of predicted clocks is not enough to meet the requirement for centimeter level applications. The IGS established the Real Time Working Group in 2001 and defined the real-time service (RTS). The RTS pilot project became operational in 2011 and provides access to precise clock correction products via Internet. The RTS products are distributed as Radio Technical Commission for Mari-time Service (RTCM)

state-space representation (SSR) correction streams and broadcast over the Internet. The accuracy of the IGS RTS satellite clocks is 0.3 ns, which meets the target of cm level in general. After the IGU orbit and RTS clock correction is transmitted to the user, the high-rate GPS data can be processed in real-time mode.

The observation equations for the GPS undifferenced (UD) carrier phase and pseudorange can be expressed as follows (Leick et al. 2015):

$$\varphi_{r,j}^{s} = \rho_{r}^{s} + dt_{r} - dt^{s} + T_{r}^{s} - I_{r,j}^{s} + \lambda_{r,j} \cdot N_{r,j}^{s} + \varepsilon_{\varphi} \tag{1}$$

$$p_{r,j}^{s} = \rho_{r}^{s} + dt_{r} - dt^{s} + T_{r}^{s} + I_{r,j}^{s} + d_{r,j} + d_{r}^{s} + \varepsilon_{p} \tag{2}$$

where the superscript s represents the GPS satellite; the subscript r and j represent the receiver and the frequency, respectively; $\varphi_{r,j}^{s}$ is the carrier phase observed at the frequency j; $p_{r,j}^{s}$ is the corresponding pseudorange; ρ_{r}^{s} denotes the geometrical range from phase centers of the satellite to receiver antennas at the signal transmitting and receiving time; dt_r is the receiver clock offset; dt^s is the satellite clock offset; T_r^s is the tropospheric delay; $I_{r,j}^{s}$ is the ionospheric delay at the frequency j; $d_{r,j}$ and d_r^s are receiver and satellite hardware delay biases; $\lambda_{r,j}$ is the wavelength of carrier phase at the frequency j; $N_{r,j}^{s}$ is the float ambiguity at the frequency j; ε_{φ} and ε_{p} are the relevant measurement noise components, including multipath of the carrier phase and pseudorange observations, respectively. Besides, the antenna phase center variations and offsets and the station displacements caused by tidal loading have to be corrected. Similarly, phase windup and relativistic delays should be corrected according to the existing models (Kouba and Hérous 2001), though they are not included in these simplified equations.

The slant total tropospheric delay can be described as the sum of the dry and wet components, and both can be expressed by their individual zenith part and mapping function. The zenith wet delay is estimated from the observations owing to the high variability of water vapor distribution and its uncertainty. The first-order ionospheric delay errors can be mitigated by the linear combination of the dual-frequency GPS observations. The ionosphere-free (IF) combination of the carrier phase and pseudoranges observables can be expressed as:

$$\varphi_{r,\mathrm{IF}}^{s} = \left(f_1^2 \cdot \varphi_{r,1}^{s} - f_2^2 \cdot \varphi_{r,2}^{s}\right) / \left(f_1^2 - f_2^2\right) \tag{3}$$

$$p_{r,\mathrm{IF}}^{s} = \left(f_1^2 \cdot p_{r,1}^{s} - f_2^2 \cdot p_{r,2}^{s}\right) / \left(f_1^2 - f_2^2\right) \tag{4}$$

Assuming that n satellites are observed at the epoch k, the observational equations for all the satellites at the epoch can be expressed as

$$L_k = A_k X_k + v_k, v_k \sim N(0, R_k) \tag{5}$$

where L is the measured output; A is the coefficient matrix; X is the state of the system; v is the measured noise; R is the measurement noise covariance.

The state equation can be expressed as

$$X_k = F_{k,k-1} X_{k-1} + w_k, w_k \sim N(0, Q_w) \tag{6}$$

where F is the state transition matrix in Kalman filter; the variable w is the process noise; Q_w is the process noise covariance.

Traditional kinematic PPP can be used to estimate the displacement waveforms, whose elements for Eq. (5) are given by

$$\begin{aligned} &L = \begin{bmatrix} \varphi_c \\ p_c \end{bmatrix}; \quad A = \begin{bmatrix} e & m_{wz} & -1 & \lambda \\ e & m_{wz} & -1 & 0 \end{bmatrix}; \\ &X = \begin{bmatrix} s & \mathrm{tro}_{\mathrm{wet}} & dt_r & N_r^s \end{bmatrix}; \quad R = \begin{bmatrix} \delta_{\varphi_c}^2 & \\ & \delta_{p_c}^2 \end{bmatrix} \end{aligned} \tag{7}$$

where φ_c and p_c are the observed minus computed carrier phase and pseudoranges observations from a satellite to the receiver; e is the unit vector from satellite to receiver; m_{wz} is the tropospheric wet mapping function; s denotes the vector of the receiver displacement correction referred to the approximate position; $\mathrm{tro}_{\mathrm{wet}}$ is the tropospheric zenith wet delay; $\delta_{\varphi_c}^2$ and $\delta_{p_c}^2$ are the noise variance for the carrier phase and pseudorange observations, respectively.

The receiver displacement correction is estimated as white noise in kinematic PPP. The tropospheric zenith wet delay is described as a random walk process. The receiver clock offset is estimated epoch-wise as white noise and the ambiguity is a constant. The process noise can be expresses as below.

$$Q_w = \tau \cdot \begin{bmatrix} m_s^2 I & 0 & 0 & 0 \\ 0 & m_z^2 & 0 & 0 \\ 0 & 0 & m_t^2 & 0 \\ 0 & 0 & 0 & 0 \end{bmatrix} \tag{8}$$

where τ is the sampling rate in seconds, I is a 3×3 identity matrix, m_s^2, m_z^2 and m_t^2 are the spectral density of displacement, troposphere and receiver clock offset noises, respectively. Here, m_s^2 is set as 100 $\mathrm{m^2\ s^{-1}}$, m_z^2 is set as 10^{-9} $\mathrm{m^2\ s^{-1}}$ and m_t^2 is set with a very large value of 10^5 $\mathrm{m^2\ s^{-1}}$.

The method of PPPVE is similar but has a little difference, which is employed for the velocity estimation by using the second-order Gaussian–Markov process in the state equations of the motion part. The L and R for Eq. (5) are the same as the elements in Eq. (7), and the A and X for Eq. (5) are expressed as (Su et al. 2019a)

$$\begin{aligned} &A = \begin{bmatrix} e & 0 & 0 & m_{wz} & -1 & \lambda \\ e & 0 & 0 & m_{wz} & -1 & 0 \end{bmatrix}; \quad X = \begin{bmatrix} s & v & a & \mathrm{tro}_{\mathrm{wet}} & dt_r & N_r^s \end{bmatrix} \end{aligned} \tag{9}$$

where v and a denote the vector of the receiver velocity and acceleration, respectively.

The station dynamics is based on the assumption that variation of position or velocity or acceleration is random. The state transition matrix and process noise matrix are expressed as following (Yang et al. 2001).

$$F = \begin{bmatrix} I & \tau I & 0.5\tau^2 I & 0 & 0 & 0 \\ 0 & I & \tau I & 0 & 0 & 0 \\ 0 & 0 & I & 0 & 0 & 0 \\ 0 & 0 & 0 & 1 & 0 & 0 \\ 0 & 0 & 0 & 0 & 0 & 0 \\ 0 & 0 & 0 & 0 & 0 & 1 \end{bmatrix} \tag{10}$$

$$Q_w = \tau \cdot \begin{bmatrix} \frac{\tau^4}{20} I q_a^2 & \frac{\tau^3}{8} I q_a^2 & \frac{\tau^2}{6} I q_a^2 & 0 & 0 & 0 \\ \frac{\tau^3}{8} I q_a^2 & \frac{\tau^2}{3} I q_a^2 & \frac{\tau^1}{2} I q_a^2 & 0 & 0 & 0 \\ \frac{\tau^2}{6} I q_a^2 & \frac{\tau^1}{2} I q_a^2 & I q_a^2 & 0 & 0 & 0 \\ 0 & 0 & 0 & m_z^2 & 0 & 0 \\ 0 & 0 & 0 & 0 & m_t^2 & 0 \\ 0 & 0 & 0 & 0 & 0 & 0 \end{bmatrix} \tag{11}$$

Here, the dynamic noise of the q_a is set 1 cm $s^{-2/5}$ and other parameters are set following Eq. (8). With the observation equations and state equations above, the parameters in PPP or PPPVE can be determined by the Kalman filter (Kalman 1960).

In PPPVE, the estimated velocities can be directly integrated into the displacements, which can be expressed as follows.

$$[s']_k = \sum_{i=k_0}^{i=k} \left([v]_i \cdot \tau + \frac{1}{2} [a]_i \cdot \tau^2 \right) \tag{12}$$

where s' is the integrated displacements and k_0 is the beginning epoch.

3 Real-time GPS velocity and displacement waveforms

The $M_w = 7.9$ earthquake occurred at 09:31:42 UTC, January 23, 2018, 37 km southeast of Kodiak, Alaska, which caused significant ground motions at distances up to several thousand kilometers from the epicenter. The University Navstar Consortium (UNAVCO) Data Center handles data management tasks for GNSS data from thousands of globally distributed permanent stations and campaign sites. A great deal of data are contributed by UNAVCO community investigators (http://www.unavco.org). The UNAVCO data center provides an ideal opportunity to evaluate the performance of co-seismic velocity and displacement waveforms derived from high-rate GPS. The 1 Hz GPS data during the 2018 Kodiak, Alaska earthquake were collected from the Plate Boundary Observatory (PBO) GNSS network, operated by UNAVCO, and we can calculate the peak ground displacement (PGD) and peak ground velocity (PGV) from the waveform traces within seconds of the earthquake. We collected IGS RTS satellite clock corrections and reprocessed those GPS data in simulated real-time mode with the method described in Sect. 2. Table 1 shows the information of the selected GPS stations including the station ID and the distance between the epicenter and each station. The distribution of the selected GPS stations and the location of the epicenter are shown in Fig. 1.

Table 1 Information of the selected GPS stations

ID	Distance (km)	ID	Distance (km)	ID	Distance (km)	ID	Distance (km)	ID	Distance (km)
AB06	910.5	AC06	436.2	AC28	695.6	AC53	649.0	AV11	455.6
AB07	716.3	AC08	427.3	AC29	420.5	AC61	979.1	AV17	461.8
AB12	825.1	AC09	513.5	AC32	620.9	AC62	808.8	AV18	459.27
AB13	583.5	AC11	652.7	AC33	752.4	AC63	859.4	AV24	1001.5
AB14	690.8	AC12	673.6	AC34	290.9	AC65	824.0	AV26	991.2
AB15	841.9	AC14	548.4	AC35	393.1	AC67	286.2	AV34	932.8
AB22	548.4	AC17	557.7	AC36	562.8	AC70	819.4	AV35	971.5
AB28	714.7	AC18	379.6	AC37	571.0	AC71	920.1	AV38	934.2
AB35	606.8	AC19	773.2	AC38	325.3	AC72	879.8	AV40	936.9
AB37	807.2	AC20	553.2	AC40	594.4	AC75	784.2	CLGO	994.6
AB42	716.1	AC21	624.0	AC43	397.7	AC77	777.8	EYAC	547.9
AB43	795.5	AC23	513.1	AC44	588.7	AC79	461.1	GRNX	876.8
AB48	899.4	AC24	544.6	AC46	684.9	AC80	731.9	SELD	417.4
AB50	920.4	AC25	836.4	AC47	503.1	ATW2	627.7	WIKR	851.2
AC02	330.4	AC26	394.3	AC51	636.1	AV01	458.1		
AC03	454.2	AC27	474.0	AC52	546.0	AV04	457.9		

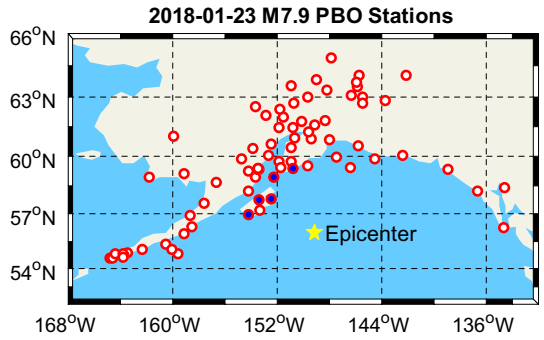

Fig. 1 Location of the 2018 Kodiak, Alaska earthquake epicenter and the distribution of the selected 1 Hz GPS stations. The epicenter is marked by the yellow star. The red circles represent 1 Hz GPS stations

The dataset of 78 1 Hz GPS stations from GPS time 07:00:00 to 11:59:59 on January 23, 2018, is processed in real-time PPPVE mode. The data are also handled in real-time PPP kinematic mode as a comparison. The satellite elevation mask angle is set to 10°. The satellite coordinates calculated by the predicted part of IGU products and clock offset derived by RTS clock correction were adopted for real-time processing. The orbit product is available at a sampling interval of 15 min. The coordinates of GPS satellites refer to "IGS14." The "igs14_1958.atx" file data generated and released by IGS was used to correct the satellite phase center offset and variation. The tropospheric delay is corrected for its dry component with the modified Hopfield model based on the meteorological parameters derived from the GPT2 model (Hopfield 1969; Lagler et al. 2013). The Vienna mapping functions (VMF) are used for the mapping functions of both the dry and wet parts according to the elevation angle of each satellite (Bohm and Schuh 2004). All remaining errors including Sagnac effect, relativity, earth tides, ocean loading and carrier phase windup are accounted for with sufficient accuracy using existing models (Petit and Luzum 2010). The precise coordinates of the stations are available in a software-independent exchange (SINEX) file provided by UNAVCO.

Figure 2 shows the comparison of displacements for a 90 min interval (07:00:00–08:29:59) prior to the earthquake at AB06 station by GPS kinematic PPP and PPPVE solution. The displacements started to be integrated 120 s after the first epoch to reduce the influence of the offset by integrating the velocity in PPPVE. It clearly shows that the GPS kinematic PPP can obtain the displacements with the accuracy of few decimetres prior to convergence. For GPS kinematic PPP solution, the coordinate parameters are correlated with the ambiguity parameters that cannot be estimated in a short time precisely and it needs approximately 30–60 min to achieve few centimeters accuracy (Su et al. 2019b). For PPPVE solution, it can quickly recover the displacements

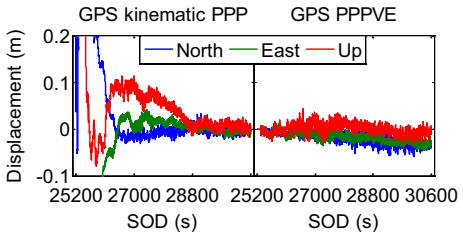

Fig. 2 The comparison of displacement for 90-min interval (07:00:00–08:29:59) at AB06 station by GPS kinematic PPP and PPPVE solution. The left side shows the GPS kinematic results and right side shows the GPS PPPVE results. The blue, cyan and red lines represent the north, east and up component, respectively

with centimeters accuracy. Though the derived coordinates may have a systematic bias compared to the true coordinates, this has no influence on displacement variation. The reason that the velocity parameters can be estimated precisely and rapidly in PPPVE is that they are not dependent on the ambiguities and just rely on the state equations.

Figure 3 depicts the distribution of the convergence time of PPPVE in unit of seconds. The velocity filter is considered to have converged when the velocity errors reach ± 0.01 m/s and keep within ± 0.01 m/s. The convergence time is the period from the first epoch to the converged epoch. The root-mean-square (RMS) and standard deviation (STD) of the convergence time are calculated as statistical indicators. The mean convergence time for north, east and up component are 19, 22 and 31 s, respectively. The results are much better than the PPP results so that the PPPVE can be used to determine the displacement in short time.

To further investigate the accuracy of velocity and integrated displacement waveforms from real-time PPPVE, a 1-h interval (UTC: 08:31:42–09:31:42) is selected before the earthquake event to calculate the velocity and displacement waveforms derived from PPPVE. The accuracy of position differences from the real-time kinematic PPP solution is also calculated as a comparison to evaluate the effect of

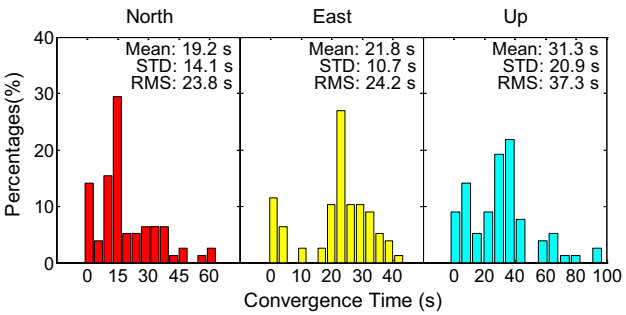

Fig. 3 Distribution of convergence time for GPS PPPVE solution using datasets collected at 78 selected 1 Hz GPS stations. The convergence time in 3 dimensions are shown in each subfigure

multipath and some other station environment-independent error sources. In order to better analyze the accuracy of the horizontal and vertical component, the coordinates and velocities are converted from the global Cartesian system into the local coordinate system (north, east and up). The displacement series in PPPVE are shifted by the difference values between the selected first epoch value and true coordinates for better analysis. The statistical results of velocities and position differences in 1-h session in the north, east and up component in PPPVE and PPP for 78 stations are summarized in Table 2. The distribution of the RMS of velocities and position differences in the north, east and up component is shown in Fig. 4. There are still systematic fluctuations of 1–2 cm in the horizontal component that could be caused by the errors of satellite orbit and clock offset and some other station environment errors in kinematic PPP solution. The RMS and STD of position difference in the vertical component is as usual larger because the height component estimates are influenced by the satellite constellation geometry and strongly correlated with tropospheric delay (Su and Jin 2018). The RMS and STD values of velocities in three components of PPPVE solution are nearly the same. The mean integrated displacement RMS values are similar to the values in kinematic PPP, which indicates that real-time PPPVE is capable of detecting seismic waveforms with a horizontal accuracy of 0.2 cm s^{-1} and a vertical accuracy of 0.4 cm s^{-1}. Kinematic PPP and PPPVE are both capable of detecting seismic displacement waveforms with amplitude of 1–2 cm horizontally and 4–5 cm vertically, whereas PPPVE can detect the displacement waveforms with much faster convergence speed.

The data of seismic waveforms can provide an insight on the dynamic rupture process of the earthquake. The 1 Hz data of stations AC67, AC38, AC02, AC18 and AC35 (marked blue in Fig. 1) were selected to analyze the horizontal displacement and velocity waveforms as the examples. The vertical components are neglected due to the large errors. The stations are arranged in terms of their distances from the epicenter to the position of the site, which are also reflected in different response times of the station movements. The displacement waveforms derived from PPP are also shown as a comparison. From Fig. 5, the systematic fluctuations are slower than the rapid position oscillations caused by the earthquake. The PPPVE displacement waveforms are consistent with kinematic PPP displacement waveforms in the horizontal components.

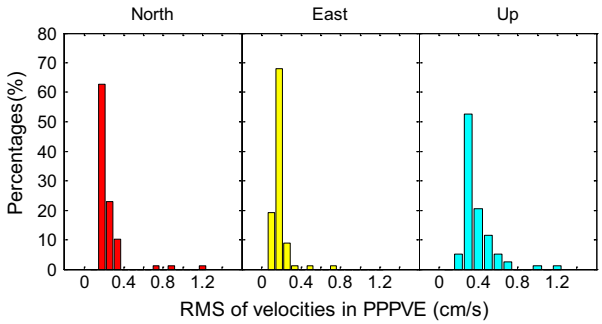

(a) Distribution of RMS of velocities in PPPVE

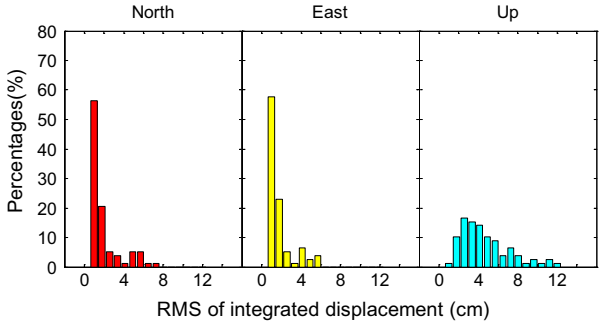

(b) Distribution of RMS of integrated displacements in PPPVE

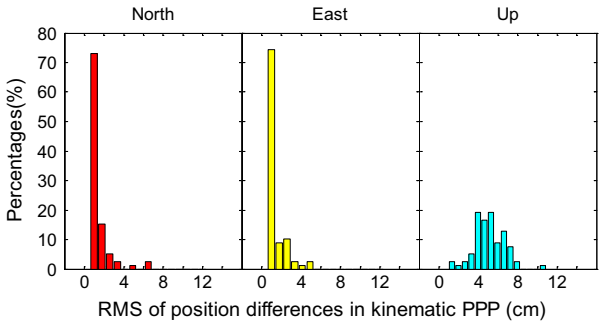

(c) Distribution of RMS of position differences in kinematic PPP

Fig. 4 Distribution of RMS errors for GPS kinematic PPP and PPPVE solution using 1-h datasets collected at 78 selected 1 Hz GPS stations (January 23, 2018 from 08:31:42 to 09:31:42). The RMS values of positioning differences and velocities in 3 dimensions are shown in each subfigure

Table 2 Statistical results including RMS and STD of velocities and position differences

Orientation and method	PPPVE				Kinematic PPP	
	Velocities (cm s^{-1})		Displacements (cm)		Displacements (cm)	
	RMS	STD	RMS	STD	RMS	STD
North	0.25	0.25	1.9	1.1	1.2	1.1
East	0.18	0.17	1.7	1.0	1.2	1.0
Up	0.38	0.38	4.7	3.2	5.1	3.9

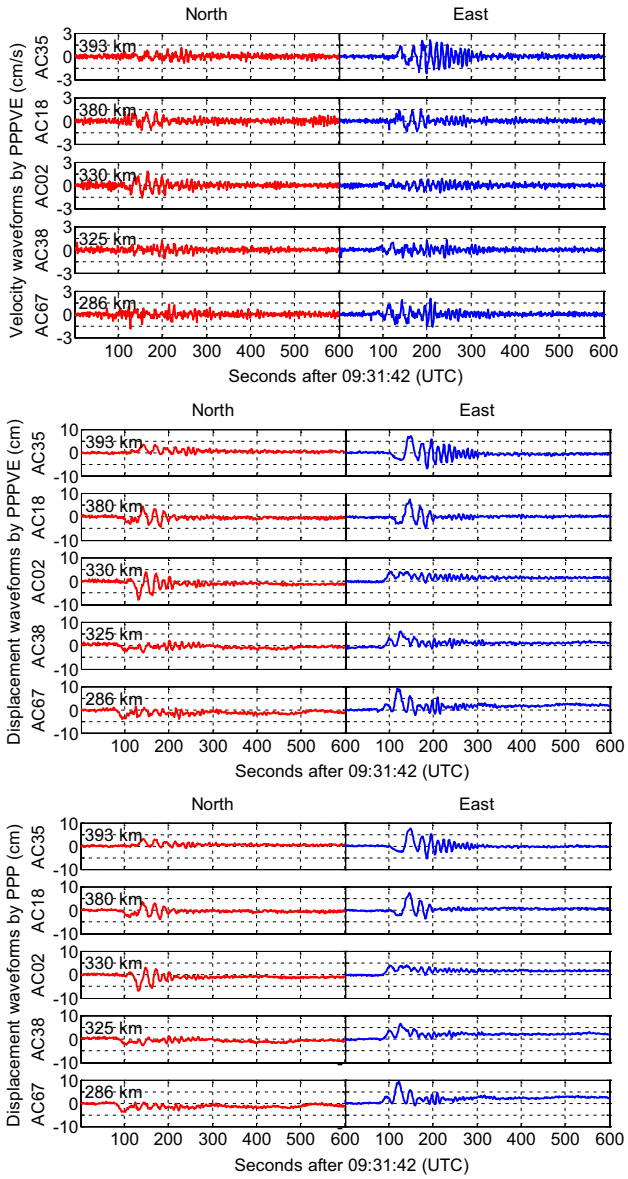

Fig. 5 Velocity and displacement waveforms by real-time PPPVE and kinematic PPP solutions at GPS stations AC67, AC38, AC02, AC18 and AC35 during the Kodiak, Alaska M_w 7.9 earthquake on January 23, 2018. The north and east components are, respectively, shown by red and green lines. The velocity and displacement waveforms in horizontal component are shown in each subfigure

Hence, the method of real-time PPPVE can easily detect the displacement and velocity waveforms in amplitude at the selected stations. In the following sections, we will employ the velocity and displacement waveforms in the horizontal components derived from real-time PPPVE to estimate the earthquake magnitude, establish the preliminary relationship between the intensity and ground motion parameters and obtain permanent displacements for the Alaska earthquake.

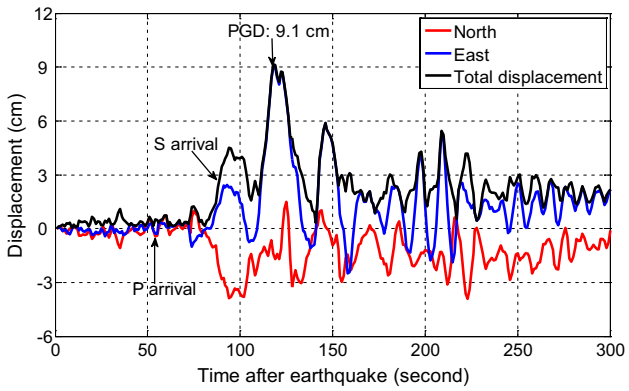

Fig. 6 GPS displacement waveforms for the measurement of peak displacement amplitude. The figure displays the north and east components of the 2018 Kodiak, Alaska earthquake by GPS site AC67 located at an epicentral distance of approximately 267 km. The peak amplitude appears at 118 s with displacement value 9.1 cm in the site. The expected arrival time of *P* wave and *S* wave is about 52 s and 89 s after the origin time, respectively

4 Seismic magnitude, density and permanent displacement

The PGDs provided by the GPS real-time PPPVE displacement waveforms are used to determine the earthquake magnitude. The horizontal peak displacement is defined as vector summation of the north and east components of the displacements. Figure 6 provides an example of extracting the PGD amplitude using the north and east components on GPS site AC67 with an epicentral distance of about 286 km. The expected arrival times of the *P* wave and *S* wave are shown in the figure. The typical values of the compressional and shear velocities in the crust ($V_P = 5.5$ km s^{-1}, $V_S = 3.2$ km s^{-1}) are used to calculate the expected arrival times of about 52 s and 89 s for *P* and *S* waves after the origin time, respectively (Stein and Wysession 2009). The maximum peak displacement amplitude appeared at 118 s after the origin time and the value is 9.1 cm, which is mainly because that the GPS peak displacement is caused by an *S* wave or surface wave rather than the *P* wave.

Earthquake magnitude is mostly used to describe the earthquake size. A number of ways can measure the magnitude of an earthquake, such as Richter scale and moment magnitude scale (Richter 1935; Hanks and Kanamori 1979). Here, we estimate the magnitude by the horizontal peak displacement derived from real-time PPPVE solution with the selected 1 Hz GPS data. The horizontal peak displacement amplitude derived from GPS data can produce information with a high signal-to-noise, where broadband seismometers clip and accelerometer data cannot provide reliable displacement. The peak displacement recorded on the receiver is closely related to the earthquake magnitude

and the epicentral distance. The general form for the magnitude scales can be defined as follow (Lay and Wallace 1995).

$$M = \lg(A/T) + a\lg(\Delta) + b \tag{13}$$

where A is the total peak horizontal displacement of the measured waves; T is the dominant period of the measured waves; a is the coefficient correction for epicentral distance Δ; and b is a constant. In general, the coefficients are determined from regression analysis of a series of events. Gutenberg (1945) deduced an empirical relationship between magnitude, peak displacement and distance based on strong-motion records of the amplitude of surface waves from a set of earthquakes occurred in California. This empirical formula is:

$$M = \lg(A) + 1.66\lg(\Delta) + 2.0 \tag{14}$$

where A is the peak horizontal displacement derived from surface waves in units of micrometer; Δ is the epicentral distance in unit of degree; and M is the earthquake magnitude.

Thus, we use Eq. (14) to calculate the earthquake magnitude using the epicentral distance and peak horizontal displacement derived from real-time PPPVE solution. Comparison between the magnitude computed with Eq. (14) and reference magnitude ($M = 7.9$) released by the U.S. Geological Survey (USGS) is shown in Fig. 7. The average value of the calculated magnitude is 7.97, and the STD is 0.18. The average deviation between the calculated magnitude and the reference magnitude is 0.07, showing a great consistency and agreement with the expected magnitude. It is worth noting that there is a small but clear trend in the magnitude estimate as a function of epicentral distance, which is not too surprising given that the coefficients used are a global average.

Furthermore, the relationship between the peak displacements and epicentral distance as a function of magnitude M can be rewritten according to Eq. (14).

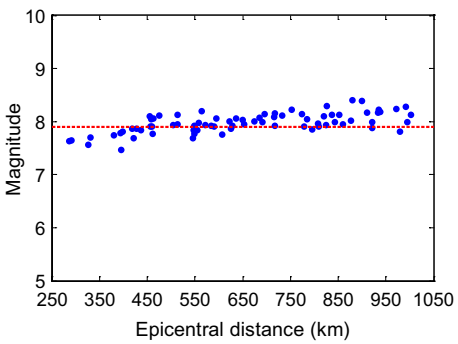

Fig. 7 Comparison between the calculated magnitude and reference magnitude released by USGS. The blue dots represent the magnitude derived from the selected 1 Hz GPS stations. The red dashed line represents the reference magnitude $M7.9$

$$A = 10^{M-2.0} \cdot \Delta^{-1.66} \tag{15}$$

To further check the suitability of the method, the expected peak displacements for magnitudes $M7.6$, $M7.9$ and $M8.2$ and the epicentral distance according to Eq. (15) are computed. The peak horizontal displacements derived from the selected stations are plotted as function of epicentral distance, which are shown in Fig. 8. It is clear that the recorded peak displacements scatter around the expected line of $M7.9$, with a slight tendency toward higher magnitude values, and the formula seems rather suitable to determine the earthquake magnitude by GPS displacement waveforms.

The seismic intensity is also an important factor to describe the damage of an earthquake. The government can focus emergency rescue response and alleviate the damage based on distribution of the seismic intensity. The relationship between the seismic intensity and ground motion parameters (PGD and PGV) can be used to estimate the

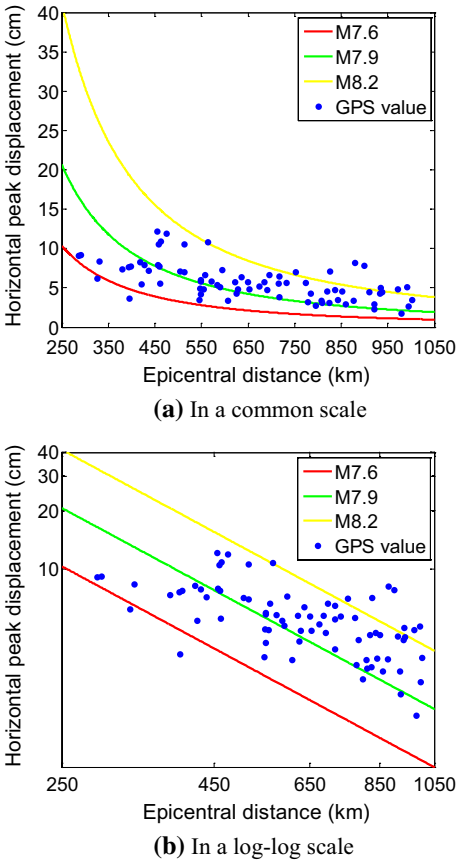

Fig. 8 Relationship between horizontal peak displacement and epicentral distance in the earthquake magnitude $M7.6$, $M7.9$ and $M8.2$. The recorded horizontal peak displacements of selected 1 Hz GPS stations are also shown by blue dots. The red, green and yellow solid lines represent the reference values of $M7.6$, $M7.9$ and $M8.2$, respectively. **a** The solid lines are lines of slope $\Delta^{-1.66}$, showing the attenuation in peak distance with epicentral distance, **b** In a log–log scale, the lines show the linear relationship with the slope of − 1.66

seismic intensity. The USGS Intensity Map relied largely on empirical ground motion prediction equations to map out shaking intensities. The USGS Community Internet Intensity system, known as "Did You Feel It" (DYFI), produced rich spatially intensity data used to augment instrumental data for Alaska earthquake. Figure 9 shows the distribution of intensity and selected GPS stations for Alaska earthquake. Only a handful of strong-motion instruments were operating during the earthquake. The GPS ground motion parameters and USGS intensity datum can be used to establish a preliminary relationship between these parameters.

The relationship between the seismic intensity and ground motion parameters can be different for each earthquake (Worden et al. 2012). There are 18 selected GPS stations in the region of intensity 2, 3, 4 and 5 altogether. The relationships between macro-intensity and PGD and PGV based on GPS data are shown in Fig. 10, which are expressed as.

$$I = 5.66 \times \lg(Dg) - 0.94 \tag{16}$$

$$I = 5.30 \times \lg(Vg) + 2.11 \tag{17}$$

where Dg and Vg are PGD and PGV values provide by real-time PPPVE, respectively. The method of extraction of PGV is similar to the method of PGD. The result shows that the peak values of GPS data can transform to the intensity of the earthquake. Considering that the statistical data is limited now, this preliminary relationship can just provide a reference for Alaska earthquake and needs more station data in the future.

In addition, the permanent displacements are obtained according to the co-seismic displacements derived from GPS real-time PPPVE solution and determined by the difference between the moment of the event and the 30 min afterward. Figure 11 displays the horizontal permanent displacements of the selected GPS stations, which proves that the PPPVE solution can fully meet the requirement for the real-time

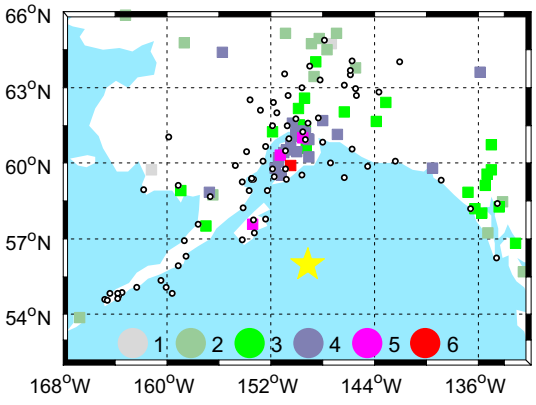

Fig. 9 Macro-intensity map for Alaska earthquake provided by USGS Community Internet system. The values of intensity (1–6) are shown by different colors

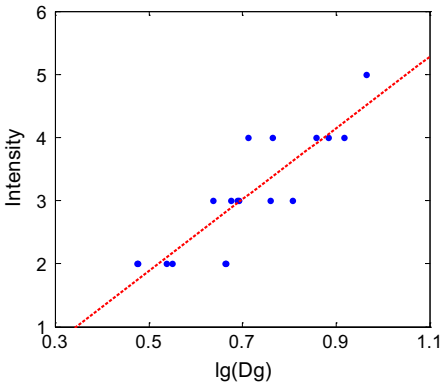

(a) The relationship between intensity and PGD

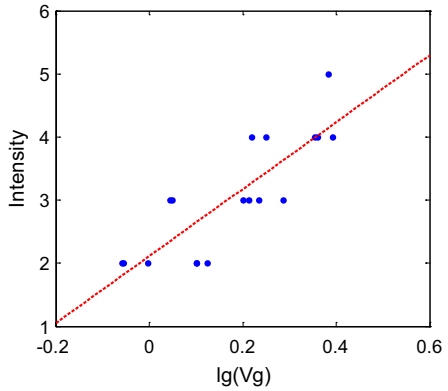

(b) The relationship between intensity and PGV

Fig. 10 The relationship between macro-intensity and PGD/PGV based on GPS data

seismic monitoring of permanent displacements. To evaluate the reliability of the derived permanent displacements from GPS real-time PPPVE solution, the final permanent displacements provided by the UNAVCO GPS Analysis Center Coordinator (ACC) (https://www.unavco.org/highl

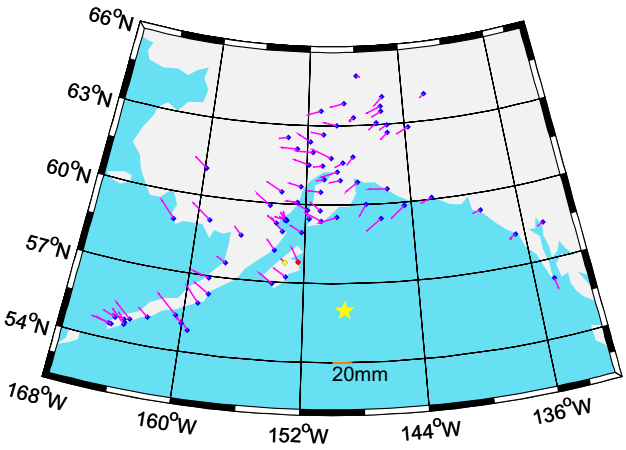

Fig. 11 Horizontal permanent displacements of the selected GPS stations derived from real-time PPPVE solution. The stations are shown in the squares. The epicenter is marked by the yellow star. The displacements in the region are shown in magenta arrows. The orange arrow is shown in the figure as the 20 mm scale for a reference

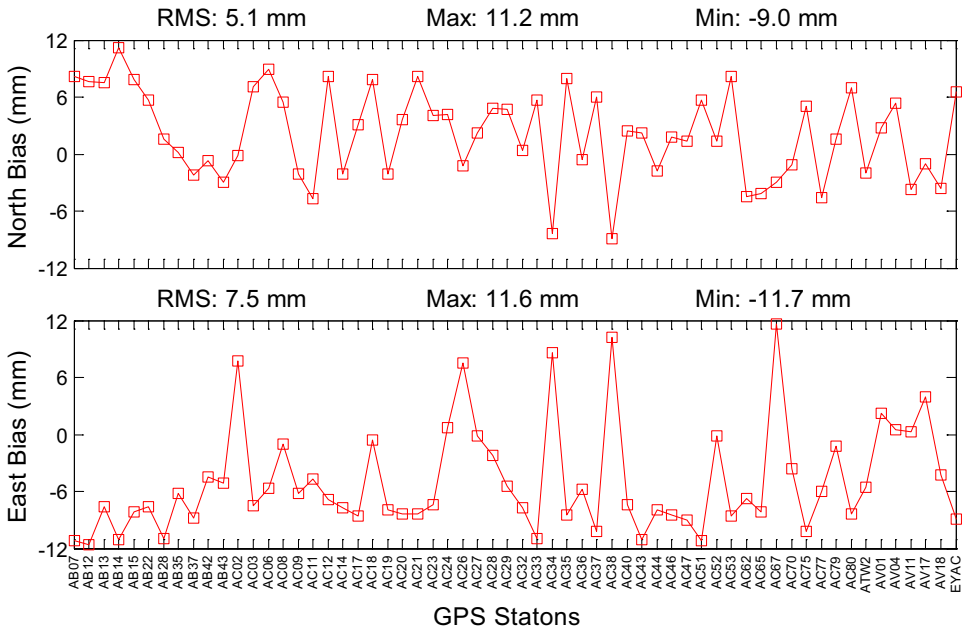

Fig. 12 The difference of PPPVE-derived displacements and the final permanent displacements for the north and east components, respectively, for 60 selected stations

ights/2018/alaska.html) are utilized, which are estimated by the accelerometer and GPS daily solution during the earthquake. Figure 12 shows the difference of PPPVE-derived displacements and the final permanent displacements for the north and east components, respectively, for 60 selected stations. Some of the stations are not shown here for their permanent displacements are not provided by the UNAVCO. The results show that the RMS values of the differences are 5.1 and 7.5 mm for the north and east components, respectively. The permanent displacements of the selected station derived from GPS real-time PPPVE are similar to the results provided by UNAVCO.

With regard to detailed displacements of the selected stations from real-time PPPVE solution, the nearest station to the epicenter, AC67, is significantly influenced by the earthquake. AC67 (marked red in Fig. 11) shifted 1.5 cm to the north and 0.7 cm to the west. The displacements of some stations closed to epicenter is not obvious. For example, AC38 (marked yellow in Fig. 11), which is 325.3 km away from the epicenter, shifted 0.4 cm to the north and 0.5 cm to the west. In total, 62.8% of the selected station shifted toward to the north and 97.4% of the stations shifted toward the west. It is evident that nearly all the stations show westward movement and the stations near the North America plate show southward movement. The reason is that the North America plate is converging with the Pacific plate toward the southwest. Since the Alaska occurred as the result of strike slip faulting within the shallow lithosphere of the Pacific plate, the orientation of faulting is consistent with trench normal compression, in which the stress field is expected for a subduction thrust environment.

5 Conclusion

The PPPVE approach for real-time GNSS seismology using a single receiver is presented. The performance of PPPVE approach is validated using 1 Hz UNAVCO data collected during the 2018, M_w 7.9 Alaska earthquake. When real-time precise orbit and clock corrections are available, the mean convergence time of PPPVE for north, east and up components are 19, 22 and 31 s, respectively. The convergence speed of PPPVE is much faster than kinematic PPP and PPPVE can be used to determine the displacement in short time. The RMS values of velocities in the north, east and up components in PPPVE solution are 0.25, 0.18 and 0.38 cm s^{-1}, respectively. The RMS values of integrated displacements in the three components are 1.9, 1.7 and 4.7 cm, respectively. The results indicate that the kinematic PPP and PPPVE are both capable of detecting seismic displacement waveforms with amplitude of 1–2 cm horizontally, whereas PPPVE can detect the displacement waveforms with faster convergence speed.

The PGDs provided by the real-time PPPVE displacement waveforms are used to determine the earthquake magnitude. The estimated magnitude of Alaska earthquake is $M_w = 7.97 \pm 0.18$, which has a great consistency and agreement with the expected magnitude. Besides, the preliminary relationship between seismic intensity and ground motion parameters is established based on the USGS intensity datum. The derived displacements are also used to obtain permanent displacements induced by the earthquake, which are similar to the UNAVCO results. Statistics show that 62.8% of the selected station shifted toward to the north and

97.4% of the stations shifted towards the west, which can be explained that that the North America plate is converging with the Pacific plate towards the southwest.

Acknowledgements This works was supported by the Startup Foundation for Introducing Talent of NUIST (Grant No. 2243141801036). We also thank the IGS for providing real-time precise orbit and clock corrections and UNAVCO for providing 1 Hz GPS data.

References

Bilich A, Cassidy JF, Larson KM (2008) GPS seismology: application to the 2002 M_w 7.9 Denali fault earthquake. Bull Seismol Soc Am 98(2):593–606

Blewitt G, Kreemer C, Hammond WC, Plag HP, Stein S, Okal E (2006) Rapid determination of earthquake magnitude using GPS for tsunami warning systems. Geophys Res Lett 33(11):L11309

Blewitt G, Hammond WC, Kreemer C, Plag HP, Stein S, Okal E (2009) GPS for real-time earthquake source determination and tsunami warning systems. J Geod 83(3–4):335–343

Bock Y, Prawirodirdjo L, Melbourne TI (2004) Detection of arbitrarily large dynamic ground motions with a dense high-rate GPS network. Geophys Res Lett 31(6):L06604

Bohm J, Schuh H (2004) Vienna mapping functions in VLBI analyses. Geophys Res Lett 31:L01603

Colosimo G, Crespi M, Mazzoni A (2011) Real-time GPS seismology with a stand-alone receiver: a preliminary feasibility demonstration. J Geophys Res Solid Earth 116(B11):B11302

Fratarcangeli F, Savastano G, D'Achille MC, Mazzoni A, Crespi M, Riguzzi F, Devoti R, Pietrantonio G (2018) VADASE reliability and accuracy of real-time displacement estimation: application to the central Italy 2016 earthquakes. Remote Sens 10(8):1201. https://doi.org/10.3390/rs10081201

Ge M, Gendt G, Rothacher MA, Shi C, Liu J (2008) Resolution of GPS carrier-phase ambiguities in precise point positioning (PPP) with daily observations. J Geod 82(7):389–399

Gutenberg B (1945) Amplitudes of surface waves and magnitudes of shallow earthquakes. Bull Seismol Soc Am 35(1):3–12

Hanks TC, Kanamori H (1979) A moment magnitude scale. J Geophys Res Solid Earth 84(B5):2348–2350

Hirahara K (1994) An experiment for GPS strain seismometer. In: Japanese symposium on GPS, pp 67–75

Hopfield HS (1969) Two-quartic tropospheric refractivity profile for correcting satellite data. J Geophys Res 74(18):4487–4499

Jin SG, Park PH (2006) Crustal stress and strain energy density rates in South Korea deduced from GPS observations. Terr Atmos Ocean Sci 17(1):169–178

Jin SG, Wang J (2008) Spreading change of Africa–South America plate: insights from space geodetic observations. Int J Earth Sci 97(6):1293–1300. https://doi.org/10.1007/s00531-007-0220-0

Kalman RE (1960) A new approach to linear filtering and prediction problems. Trans ASME 82:35–45

Keller RJ, Nichols ME, Lange AF (2001) U.S. patent no. 6,199,000. U.S. Patent and Trademark Office, Washington, DC

Kouba J (2003) Measuring seismic waves induced by large earthquakes with GPS. Stud Geophys Geodyn 47:741–755

Kouba J (2005) A possible detection of the 26 December 2004 great Sumatra–Andaman islands earthquake with solution products of the international GNSS service. Stud Geophys Geodyn 49:463–483

Kouba J, Héroux P (2001) Precise point positioning using IGS orbit and clock products. GPS Solut 5(2):12–28

Lagler K, Schindelegger M, Böhm J, Krásná H, Nilsson T (2013) GPT2: empirical slant delay model for radio space geodetic techniques. Geophys Res Lett 40(6):1069–1073

Larson KM, Bodin P, Gomberg J (2003) Using 1-Hz GPS data to measure deformations caused by the Denali fault earthquake. Science 300(5624):1421–1424

Lay T, Wallace TC (1995) Modern global seismology, vol 58. Academic Press, Cambridge

Leick A, Rapoport L, Tatarnikov D (2015) GPS satellite surveying, 4th edn. Wiley, Hoboken

Li X, Ge M, Guo B, Wickert J, Schuh H (2013) Temporal point positioning approach for real-time GNSS seismology using a single receiver. Geophys Res Lett 40(21):5677–5682

Li X, Zhang X, Ren X, Fritsche M, Wickert J, Schuh H (2015) Precise positioning with current multi-constellation global navigation satellite systems: GPS, GLONASS, Galileo and Beidou. Sci Rep 5:8328

Ohta Y, Kobayashi T, Tsushima H, Miura S, Hino R, Takasu T, Sato T (2012) Quasi real-time fault model estimation for near-field tsunami forecasting based on RTK-GPS analysis: application to the 2011 Tohoku-Oki earthquake (M_w 9.0). J Geophys Res Solid Earth 117(B2):B02311

Petit G, Luzum B (eds) (2010) IERS Conventions (2010), IERS technical note 36. Verlagdes Bundesamtsfür Kartographie und Geodäsie, Frankfurt am Main

Remondi BW (1985) Performing centimeter-level surveys in seconds with GPS carrier phase: initial results. Navigation 32(4):386–400

Richter CF (1935) An instrumental earthquake magnitude scale. Bull Seismol Soc Am 25(1):1–32

Shi C, Lou Y, Zhang H, Zhao Q, Geng J, Wang R, Fang R, Liu J (2010) Seismic deformation of the M_w 8.0 Wenchuan earthquake from high-rate GPS observations. Adv Space Res 46:228–235

Stein S, Wysession M (2009) An introduction to seismology, earthquakes, and earth structure. Wiley, Hoboken, p 60

Su K, Jin S (2018) Improvement of multi-GNSS precise point positioning performances with real meteorological data. J Navig 71(6):1363–1380. https://doi.org/10.1017/S0373463318000462

Su K, Jin S, Ge Y (2019a) Rapid displacement determination with a stand-alone multi-GNSS receiver: GPS, Beidou, GLONASS, and Galileo. GPS Solut 23(2):54

Su K, Jin S, Hoque MM (2019b) Evaluation of ionospheric delay effects on multi-GNSS positioning performance. Remote Sens 11(2):171. https://doi.org/10.3390/rs11020171

Tu R (2013) Fast determination of displacement by PPP velocity estimation. Geophys J Int 196(3):1397–1401

Worden CB, Gerstenberger MC, Rhoades DA, Wald DJ (2012) Probabilistic relationships between ground-motion parameters and modified Mercalli intensity in California. Bull Seismol Soc Am 102(1):204–221

Wright TJ, Houlié N, Hildyard M, Iwabuchi T (2012) Real-time, reliable magnitudes for large earthquakes from 1 Hz GPS precise point positioning: the 2011 Tohoku-Oki (Japan) earthquake. Geophys Res Lett 39(12):L12302

Xu P, Shi C, Fang R, Liu J, Niu X, Zhang Q, Yanagidani T (2013) High-rate precise point positioning (PPP) to measure seismic wave motions: an experimental comparison of GPS PPP with inertial measurement units. J. Geod 87:361–372

Yang Y, He H, Xu G (2001) Adaptively robust filtering for kinematic geodetic positioning. J Geodesy 75(2–3):109–116

Zhang X, Li X, Guo F (2011) Satellite clock estimation at 1 Hz for realtime kinematic PPP applications. GPS Solut 15(4):315–324

Zumberge JF, Heflin MB, Jefferson DC, Watkins MM, Webb FH (1997) Precise point positioning for the efficient and robust analysis of GPS data from large networks. J Geophys Res 102(B3):5005–5017. https://doi.org/10.1029/96JB03860